High Fe content in Al-Mg-Si wrought alloys facilitates excellent mechanical properties

Bernhard Trink [a],[*], Irmgard Weißensteiner [a], Peter J. Uggowitzer [b], Katharina Strobel [c], Stefan Pogatscher [a]

[a] Christian Doppler Laboratory for Advanced Aluminum Alloys, Chair of Nonferrous Metallurgy, Montanuniversität Leoben, Franz-Josef-Straße 18, 8700 Leoben, Austria
[b] Chair of Nonferrous Metallurgy, Montanuniversität Leoben, Franz-Josef-Staße 18, 8700 Leoben, Austria
[c] AMAG rolling GmbH, Postfach 32, 5282 Ranshofen, Austria

ARTICLE INFO

ABSTRACT

This study investigates the effect of a high volume fraction of Fe-rich intermetallic phases on microstructure evolution and mechanical properties in a cold rolled Al-Mg-Si wrought alloy. A conventional Al-Mg-Si alloy was modified by significantly increasing its Fe and Mn content, while the Si content was adjusted to keep the matrix composition comparable. Subsequent fast solidification and thermomechanical processing generated a dense distribution of fine intermetallic phases, which culminated in significant grain-refinement and uniform texture. The resulting alloy, with almost 10 vol-% Fe-rich intermetallic phase, features an unusually attractive combination of strength and ductility in addition to the substantially increased strain hardening typical of heterostructured materials, and can facilitate a higher usage of scrap input.

A major challenge in the recycling of aluminum is the highly diverse composition of aluminum scrap. Among other elements, Fe poses a particular problem as (i) it gradually accumulates through the recycling of secondary aluminum and (ii) it is difficult to remove by metallurgical means [1,2]. Due to the low solubility of Fe in the aluminum solid solution (<0.05 wt.%), it tends to form primary phases during the casting process [3]. The effect of Fe in aluminum casting alloys has already been studied extensively [4–7]. The most important Fe-rich primary intermetallic phases (hereafter "IMPs") in aluminum alloys containing Si are α-AlFeSi and β-AlFeSi [5]. The α-phase is characterized by a much more compact morphology than that of the plate-like β-phase [8,9]. For this reason, because of its influence on mechanical properties, α-AlFeSi is preferred [1]. Most of the Fe-rich primary IMPs are known to reduce ductility and to negatively affect formability [3]. Modifying their structure and morphology (e.g by adding Mn [10–12]) might reduce their negative effects. In addition, fast solidification (>10 K/s) is known to promote beneficial formation of refined α-AlFeSi instead of β-AlFeSi [1,13], with a higher solidification rate required at higher Fe content. Iron-rich IMPs can also be fragmented and converted to more rounded shapes by heat treatments [14,15]. Homogenization between 530°C and 600°C triggers the transformation of plate-shaped β-particles to globular α-particles, which is known to improve formability and prevent localized cracking and surface defects [10,12,16].

Interestingly, foil materials (i.e. 8xxx alloys [17]) typically have a very high Fe content and exhibit good elongation and forming properties. Recently a study in the context of other Al alloys showed that a crossover between different classes of alloys offers great potential in terms of combining positive properties (i.e. good formability and high strength were seen for a crossover between 5xxx and 7xxx alloys in [18]). Inspired by this, we aimed for a crossover between 6xxx and Fe-rich 8xxx series alloys.

In this study we demonstrate that a purposely generated high volume fraction of hard iron-rich IMPs can be used to positively influence grain size, final material properties, and recyclability. The concept shows hetero-deformation-induced (HDI) strengthening and HDI strain hardening to improve mechanical properties [19,20] of the final sheet characteristics of Al-Mg-Si wrought alloys with high Fe-content.

To synthesize the test alloy with high IMP content, the alloy EN-AW 6016 containing 1.2% Si, 0.4% Mg, 0.2% Fe and 0.1% Mn, which served as a reference, was remelted, and Mn (75% Mn and 25% Al reagent), Fe (75% Fe and 25% Al reagent) and Si (100% Si reagent) were added via master alloys (contents given in wt.%). The chemical composition of the test alloy with high IMP content (6016+IMPs) exhibit the following values: 1.9% Si, 0.4% Mg, 1.4% Fe and 1.1% Mn. In addition to the
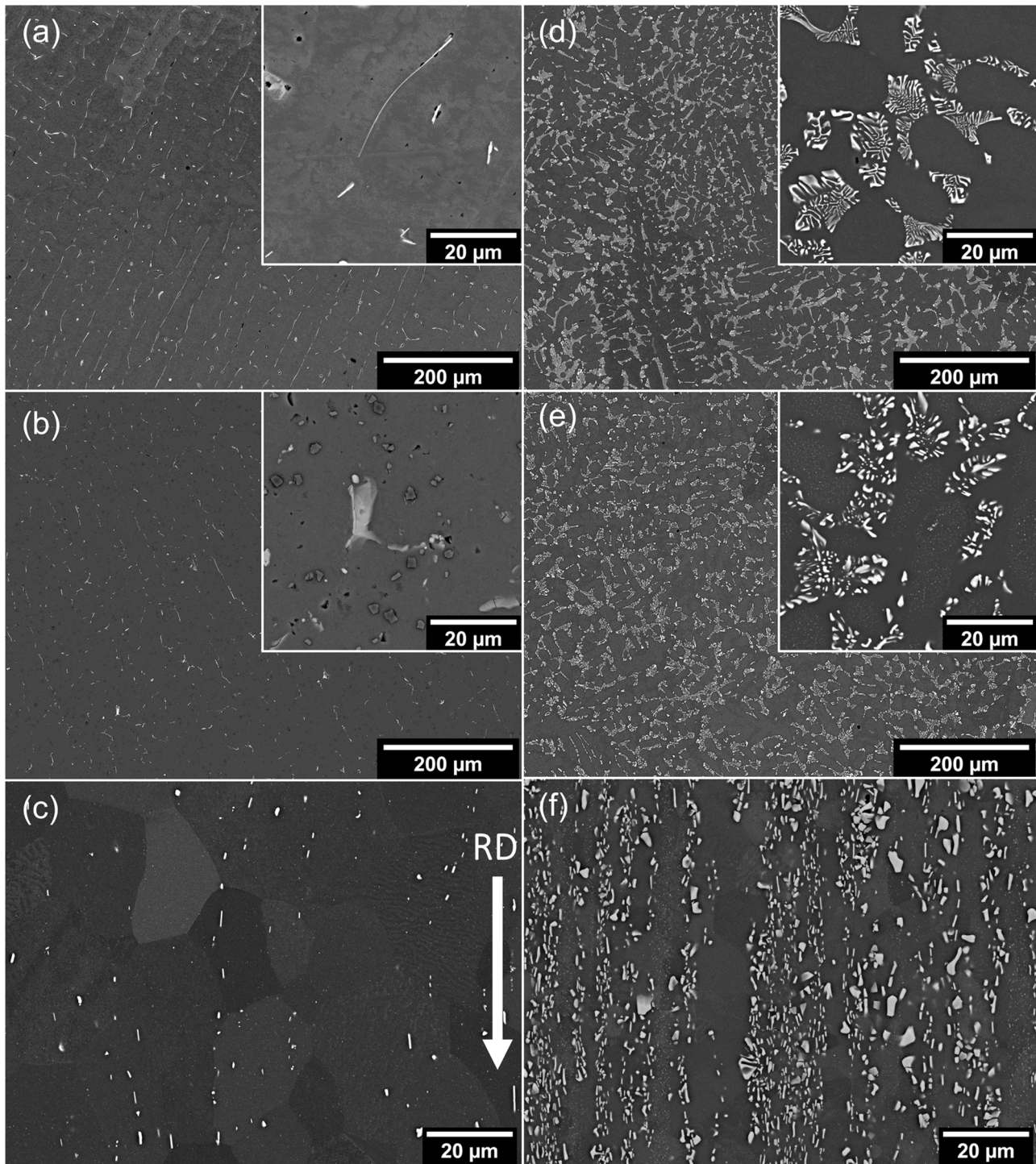
Fig. 1. BSE micrographs of reference alloy 6016 (a-c) and alloy 6016+IMPs (d-f) in the conditions as-cast (a,d), homogenized (b,e) and solution annealed (c,f).

increase in Fe and Mn, the Si content was deliberately increased to account for its incorporation into IMPs and to enable a similar amount of dissolved Mg and Si at the solution treatment temperature (calculated by FactSage 8.0 database FTlite). The alloys were subjected to similar processing procedures: remelting and alloying of the elements in an induction furnace; casting into a rectangular copper mold as described in [21] (cooling rate $\approx$ 60°C/s, capacity of 100 g); homogenization treatment at 560°C with a heating period of 8h, followed by a holding time of 11h; hot-rolling with a laboratory rolling mill from 12 mm to 7.3 mm and cold rolling to 1.2 mm sheet thickness, with intermediate annealing at 560°C for 25 minutes at 3.1 mm; and finally solution heat

treatment at 560°C for 2 minutes in a contact press, with subsequent quenching in water at RT.

Tensile tests were performed directly after solution heat treatment and after 16 days of natural aging at room temperature using a Zwick/ Roell Z 100 model tensile testing machine with a gauge length for the samples of 45 mm and a crosshead speed of 0.0032 mm/s in the rolling direction. For microstructural analysis the cross-section planes of the sheet material (rolling and normal direction) were prepared by standard metallographic procedures. Microstructural analysis was performed on a scanning electron microscope (SEM) type JEOL-7200F. The evaluation of the IMPs was carried out using the software package ImageJ. Electron

Table 1

Microstructural characteristics of reference alloy 6016 and the alloy 6016+IMPs after solution annealing

IMPs	6016	6016+IMPs
Area fraction [%]	0.5	9.1
Mean equivalent circular diameter [nm]	650 ± 360	780 ± 495
Number of analysed particles [-]	817	10150
Dispersoids		
Area fraction [%]	0.02	0.10
Mean equivalent circular diameter [nm]	96 ± 41	112 ± 48
Number of analysed particles [-]	77	281
Grain size		
Average equivalent diameter [μm]	22.5 ± 10.4	6.9 ± 3.5
Mean aspect ratio [-]	1.76 ± 0.54	1.62 ± 0.45

backscattered diffraction (EBSD) was performed using a Symmetry S2 detector from Oxford Instruments. For data analysis, the software package Aztec Crystal and the mtex toolbox were utilized [22]. The orientation distribution functions were evaluated as described in [23].

The results of the microstructural evaluation are shown in Fig. 1 for both alloys, 6016 (a-c) and 6016+IMPs (d-f). In the as-cast condition (central area), the IMPs in the reference 6016 alloy (Fig. 1 a) are mostly fine and elongated in shape, while homogenization (Fig. 1 b) entails a certain degree of curvature (darker structures seen in the insert of Fig. 1 b are artefacts from metallographic preparation). In alloy 6016+IMPs (Fig. 1 d), the morphology resembles that of an Al-α-AlFeSi eutectic with a twisted arm structure. This "Chinese script" morphology forms by coupled growth via a binary eutectic reaction with the α-Al-phase [5]. The EBSD analyses reveal a cubic structure. This crystal structure, together with the twisted arm morphology, are strong indications for the α-AlFeSi phase [1]. Thermodynamic simulations with the FactSage 8.0 software package and EDS measurements also support the evidence of α-Al(Fe,Mn)Si phases. For both, 6016 and 6016+IMPs, primary silicon was not detected in as cast condition. The homogenization treatment induces distinct changes in the morphology of the primary phases (Fig. 1
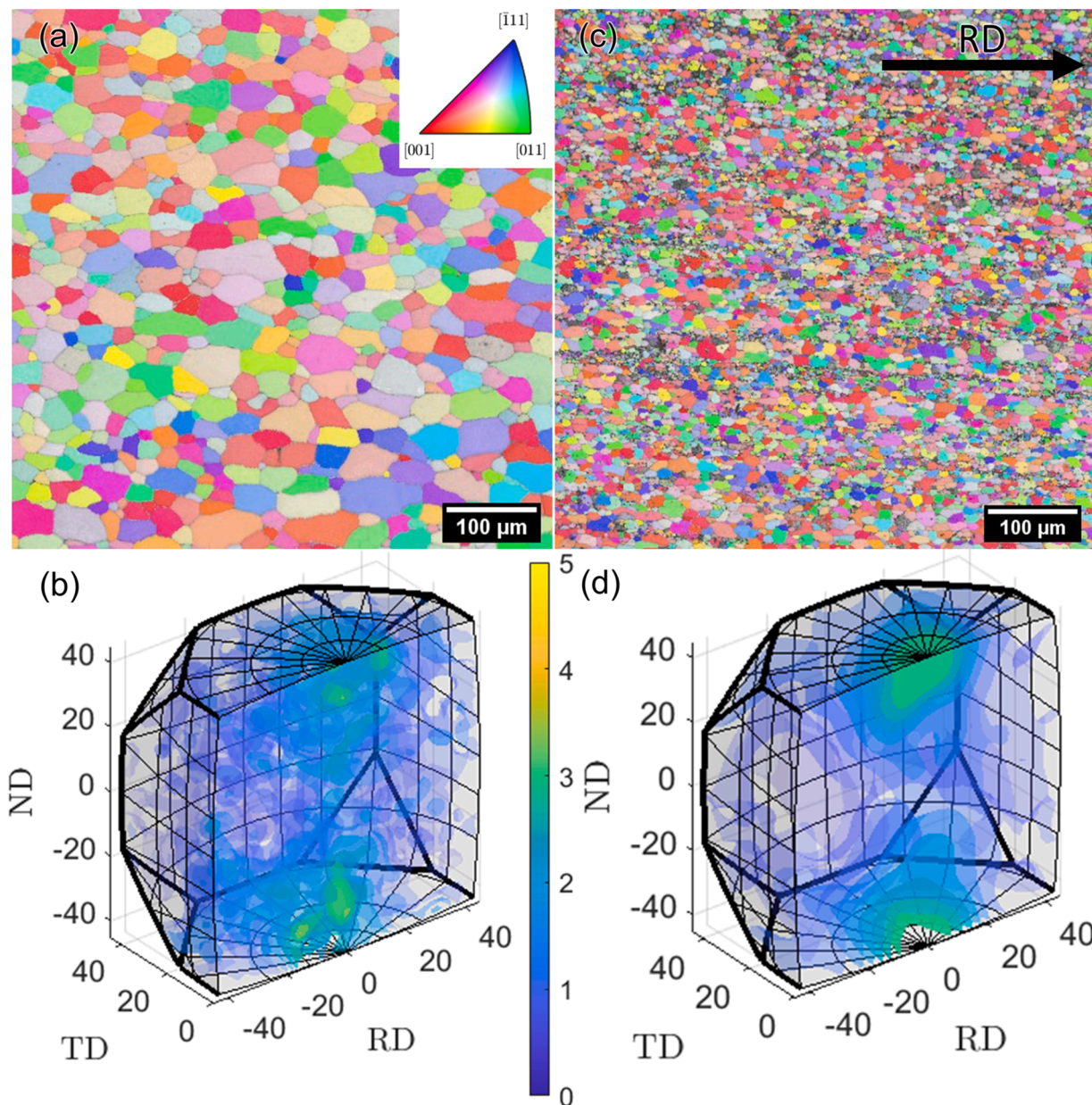

Fig. 2. IPFZ maps (a, c) of the solution treated alloy sheets transverse to the rolling direction (RD) and the ODFs (b, d) of reference alloy 6016 (a, b) and alloy 6016+IMPs (c, d) in the axis/angle space.
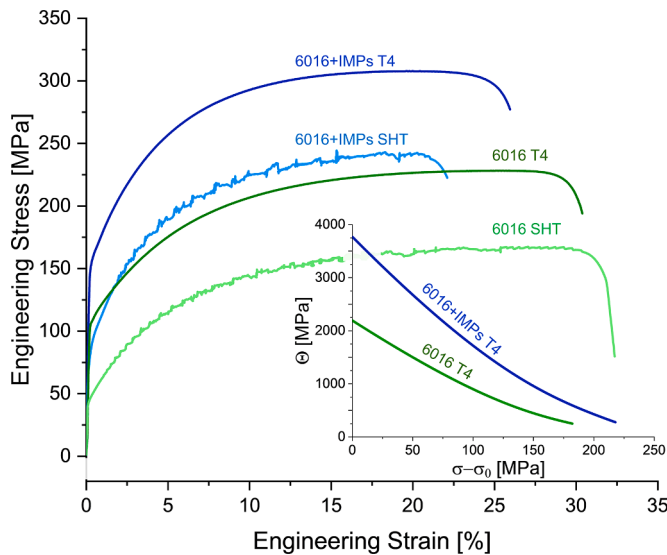
Fig. 3. Engineering stress-strain curves for alloy 6016+IMP and reference alloy 6016 in as quenched (SHT) and T4 (16 days of natural aging) condition. The insert shows a "Kocks-Mecking plot" of the data [6016 and 6016+IMP], displaying the hardening rate in dependence on the true stress beginning at the yield point.

Table 2
Mechanical properties of alloys 6016 and 6016+IMP in the conditions T4 and SHT.

	6016 (SHT)	6016 (T4)	6016+IMP (SHT)	6016+IMP (T4)
$R_{p0,2}$ [MPa]	48 ± 1	110 ± 1	86 ± 1	159 ± 1
R_m [MPa]	167 ± 1	229 ± 1	246 ± 2	308 ± 1
A_g [%]	24.1 ±2.9	24.3 ± 1.1	17.6 ± 2.1	19.0 ± 0.6
A [%] *	32.2 ± 2.8	30.1 ± 1	21.8 ± 2.2	24.7 ± 1

e). Besides a coarsening of the previously fine lamellar structure, a fragmentation into individual particles is evident. After rolling and solution annealing (Fig. 1 f), the IMPs in 6016+IMPs feature a refined shape with rounded edges. On average, the area fraction of the IMPs in 6016+IMPs is 9.1% and the calculated mean equivalent circular diameter is 780±495 nm (note: to avoid including fine secondarily precipitated particles and dispersoids in the evaluation of IMPs, only particles with an equivalent circular diameter >200 nm were used for the calculation of the mean equivalent circular diameter). In comparison, the area fraction of reference alloy 6016 (Fig. 1 c) is less than 0.5 %. As expected, the rolling process aligned the IMPs in the rolling direction.

The secondary dispersoids after solution annealing exhibit a globular morphology with a size of about 112±48 nm (equivalent circular diameter) in alloy 6016+IMPs and 96±41 nm in reference alloy 6016. The high standard deviation results from the fact that the primary phases are fragmented to very different sizes as shown in Fig. 1. The quantity of dispersoids in the experimental alloy 6016+IMPs is also much higher than in the standard 6016 alloy, because Mn also contributes to their formation [11,24]. Table 1 summarizes the most important microstructural features.

Fig. 2 illustrates the pronounced difference in microstructure between 6016 and 6016+IMPs. By means of EBSD, the crystal orientations were determined and plotted as inverse pole figure maps. Both alloys are completely recrystallized after the solution heat treatment. We attribute the refinement of the microstructure in the 6016+IMP variant to enhanced nucleation rate during recrystallization via particle stimulated nucleation (PSN) [15,25,26]. In the neighbourhood of IMPs an increased dislocation density is formed during rolling, creating favourable sites for the formation of recrystallization nuclei [15]. In parallel, the large number of interfaces (originating from both the IMPs and the dispersoids) hinders coarsening of the newly formed grains [25–29]. Consequently, the finest grains, with sizes below 5 µm, are found in areas of high particle density. New grains generated by particle stimulated nucleation have certain orientations, which are independent for each individual particle [25]. If PSN dominates the recrystallization process it induces more random orientations, which lead to a rather weak texture on the macroscale [25]. Both alloys exhibit a weak texture (6016, J-Index: 1.3536 and 6016+IMPs, J-index: 1.3006); the only visible increase in orientation densities is the cube orientation rotated 45° around

the normal direction (Euler angles 0°-45°-0° in Bunge convention). In 6016+IMPs this orientation is more pronounced. Fig. 2 (b) (6016) and (d) (6016+IMPs) show the respective orientation distribution functions in the axis-angle space. In both cases, orientations of well over 3000 grains were evaluated.

Fig. 3 presents the technical stress-strain curves from tensile tests of the 6016 and 6016+IMPs (values are given in Table 2). Two unique features are particularly striking: on the one hand the significantly higher strength values of alloy 6016+IMPs, and on the other its simultaneous surprisingly high total elongation of ≈ 25%.

We will first assess the higher strength values of alloy 6016+IMPs in both SHT and T4. Comparing the increase in yield strength from the solution-annealed condition (SHT) with T4, we notice that natural aging is about 11 MPa greater in alloy 6016+IMPs. Although the matrix composition upon solution treatment was adjusted via FactSage this may come about due to slight deviations in Mg and Si arising from the melting process or uncertainties in the FactSage simulation. The increase in yield strength of alloy 6016+IMPs of ≈ 38 MPa in SHT condition can be attributed to the interaction of multiple mechanisms. Increased solid solution hardening may have a small influence, but the contributions to strength increase result primarily from increased grain boundary hardening and the formation of geometrically necessary dislocations (GNDs), which can be assigned to hetero-deformation-induced (HDI) strengthening [19].

The increase in boundary hardening is quite obvious. For the refined grains in alloy 6016+IMPs (the grain size of 6.9 µm is significantly smaller than that of alloy 6016 with 22.5 µm), a yield strength increase of about 13.6 MPa is calculated according to Hall-Petch with a k_y of 80 MPa$\sqrt{(\mu m)}$ [30].

The HDI strengthening via the formation of GDN is attributed to two key issues. Firstly, the difference in thermal expansion between the Al matrix and the IMPs, and secondly, the fact that the IMPs do not deform plastically. In both cases we apply Ashby's concept [31] and determine the number of dislocation loops, *n*, necessary to compensate for the geometric mismatch between matrix and IMPs.

We first consider the situation when quenching from the solution heat treatment temperature. With an IMP size of *d* and a difference in the coefficient of thermal expansion $\Delta\alpha$ between the Al matrix and the IMPs, we obtain the number of GNDs formed upon quenching according to $n = A\frac{\Delta\alpha\Delta Td}{b}$ [30]. With $\Delta\alpha \approx 14 \times 10^{-6}$ K^{-1} [32], b=0.29 nm (b Burgers vector of Al), $A=3$ for cube-shaped particles and $\Delta T= 540$ K (quenching from 560°C to RT) one calculates 78 dislocations per intermetallic particle. Assuming a particle size of ≈ 1 µm and a volume fraction of ≈ 10 %, these dislocations are to be assigned to an area of ≈ 10 µm^2, which corresponds to a dislocation density ρ of 7.8×10^{12} m^{-2}. Using the Taylor equation [33], $\sigma = \alpha Gb\sqrt{\rho}$ (G shear modulus, 25.5 GPa; $\alpha \approx 0.6$) an increase in yield strength of approximately 12 MPa is calculated.

We now apply the concept of Ashby [31] to assess the stress increase caused by the presence of IMPs that do not deform plastically. First, we estimate the dislocation loops required to compensate for the volume difference resulting from the plastic deformation of the Al matrix compared to the undeformed IMPs. For cubic particles of size *d,* the number of geometrically necessary dislocations loops results in: $n = A\frac{\varepsilon d}{b}$ (ε amount of plastic deformation). Considering the volume fraction f_V of IMPs, the following relationship is obtained for the dislocation density:
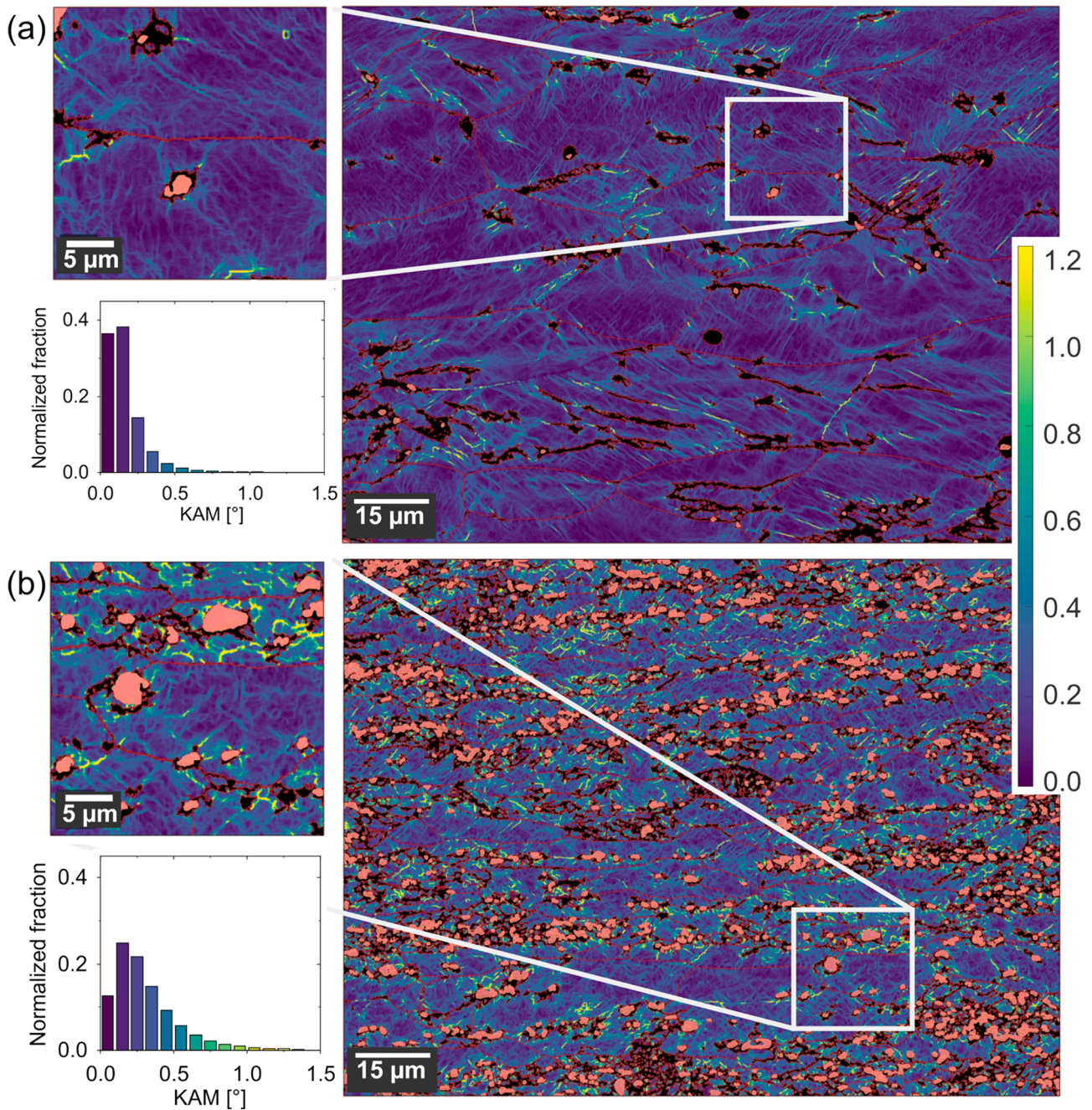
Fig. 4. EBSD kernel average misorientation (KAM), grain boundaries >10° (red) and IMPs (red) of (a) alloy 6016 and (b) alloy 6016+IMPs after applying 25% strain. The insert shows a magnified section of the micrograph; the histograms quantify the distribution of the individual KAM values, with a shift to higher KAM for 6016+IMPs (total normalized fraction = 1).

$\rho = \frac{8\varepsilon f_V}{bd}$. Now we consider that at the measured yield strength, $R_{p0.2}$, the material is 0.2% plastically deformed. With a particle size of 1 μm, a plastic deformation of 0.2% and a volume fraction of 10%, the GND density is calculated as $\approx 5.5 \times 10^{12}$ m^{-2}. Using the Taylor equation, the corresponding increase in yield strength calculates to $\approx$10 MPa. Thus, all the individual contributions to the yield strength increase add up to a value of approximately 35.5 MPa, which is in good agreement with the measured values.

At this point we must note, that the formation of GNDs around rigid IMPs and the associated hardening is equivalent to increased strain hardening in the regime of plastic deformation. As shown in the insert to Fig. 3 ("Kocks-Mecking plot"), the strain hardening is much more pronounced in 6016+IMPs. This can be illustrated by a simple example: A plastic deformation of 2% results in an additional flow stress increase in 6016+IMPs in T4 of approximately 30 MPa compared to 6016 (note the different slope of the σ−ε plot in Fig. 3). Now we calculate the above example for increasing GND density caused by plastic deformation again, but now for 2% deformation. The result is a value of $\approx 5.5 \times 10^{13}$ m^{-2}, which corresponds to a strength increase of 33 MPa. This increased strain hardening agrees quite well with the measured stress increase of 30 MPa. We thus conclude, in agreement with the literature [19,20], that the heterogeneous microstructure of alloy 6016+IMPs positively affects strength properties.

We will now assess possible explanations for the remarkably good ductility, demonstrated by the appearance of necking strain and an elongation to fracture of approx. 25%. For this purpose, we first consider

the kernel average misorientation (KAM, 1st order, step size 80 nm, threshold 5°) of the Al-matrix after applying a tensile strain of 25% for the 6016 and 6016+IMPs in T4 condition in Fig. 4 (note: for 6016+IMPs this is close to the elongation to fracture). The KAM values can be seen as a measure of GND density or local misorientation. In graphical visualization the color range is spanned between 0° and 1.2°; higher misorientation values are indicated with the brightest color. The areas detected as intermetallic particles are colored in red. If we compare the two structures, more lattice deformation (caused by GNDs) is observable in alloy 6016+IMPs, and it is preferentially concentrated around primary phases to accommodate the global strain. The KAM histograms also show that in line with the increased strain hardening discussed above, the distribution is broader and shifted to higher KAM values for alloy 6016+IMPs. It is also interesting to note that no zones of local deformation in the form of narrow shear bands are visible. Non-uniform deformation within such zones would lead to premature fracture due to the growth and coalescence of cavities [34]. Such cavities are generally caused by the cracking of coarse second-phase particles, especially Fe-rich IMPs with high aspect ratios [35], or the decohesion of the matrix from second-phase particles due to dislocation pile-up stresses at the particle-matrix interface [36]. In each of the possible cases, the small size and spherical morphology of the IMPs, as well as the small matrix grain size and the GND forest surrounding the particles, help to prevent the early formation of pores and thus failure.

In summary, a new Al-Mg-Si alloy system with a high fraction of Fe-rich primary intermetallic phases was created. We note that new wrought alloys containing tramp elements which exceed current standards have considerable potential. The positive effects of the emerging heterostructure comprise significantly smaller grains than those of reference alloy 6016, plus higher strength and higher strain hardening generated by the formation of geometrically necessary dislocations. The surprisingly high total elongation in tensile tests can be attributed to the effects of IMP refinement and morphology, grain refinement and a more uniform deformation. However, the morphological control of Fe-rich primary intermetallic phases through appropriate processing is crucial for the success of such a strategy.

Declaration of Competing Interest

The authors declare that they have no known competing financial interests or personal relationships that could have appeared to influence the work reported in this paper.

References

[1] L. Zhang, J. Gao, L.N.W. Damoah, D.G. Robertson, Mineral Processing and Extractive Metallurgy Review 33 (2012) 99–157.
[2] J.A.S. Green, Aluminum Recycling and Processing for Engergy Conservation and Sustainability, A S M International, Materials Park, 2007.
[3] L.F. Mondolfo, Aluminium alloys: Structure and properties, Butterworth, London, Boston, 1979.
[4] S. Ji, W. Yang, F. Gao, D. Watson, Z. Fan, Materials Science and Engineering: A 564 (2013) 130–139.
[5] Z. Que, Y. Wang, Z. Fan, Metall Mater Trans A 49 (2018) 2173–2181.
[6] D. Wang, H. Zhang, H. Nagaumi, X. Li, J. Cui, Adv. Eng. Mater. 22 (2020), 2000517.
[7] M.A. Moustafa, Journal of Materials Processing Technology 209 (2009) 605–610.
[8] C.M. Dinnis, J.A. Taylor, A.K. Dahle, Scripta Materialia 53 (2005) 955–958.
[9] L. Lu, A.K. Dahle, Metall Mater Trans A 36 (2005) 819–835.
[10] N. Kuijpers, F.J. Vermolen, C. Vuik, P. Koenis, K.E. Nilsen, S. van der Zwaag, Materials Science and Engineering: A 394 (2005) 9–19.
[11] M.S. Remøe, K. Marthinsen, I. Westermann, K. Pedersen, J. Røyset, C. Marioara, Materials Science and Engineering: A 693 (2017) 60–72.
[12] S. Zajac, B. Hutchinson, A. Johansson, L.-O. Gullman, Materials Science and Technology 10 (1994) 323–333.
[13] S. Belmares-Perales, Met. Mater. Int. 14 (2008) 307–314.
[14] J. Grasserbauer, I. Weißensteiner, G. Falkinger, T.M. Kremmer, P.J. Uggowitzer, S. Pogatscher, Materials (Basel, Switzerland) 14 (2021) 3204.
[15] E. Aryshenskii, J. Hirsch, S. Konovalov, Metals 11 (2021) 507.
[16] N. Kuijpers, W.H. Kool, P. Koenis, K.E. Nilsen, I. Todd, S. van der Zwaag, Materials Characterization 49 (2002) 409–420.
[17] M. Lentz, G. Laptyeva, O. Engler, Journal of Alloys and Compounds 660 (2016) 276–288.
[18] L. Stemper, M.A. Tunes, R. Tosone, P.J. Uggowitzer, S. Pogatscher, Progress in Materials Science (2021), 100873.
[19] Y. Zhu, Metall Mater Trans A 52 (2021) 4715–4726.
[20] L. Lu, X. Wu, I.J. Beyerlein, Scripta Materialia 187 (2020) 307–308.
[21] F. Schmid, L. Stemper, T. Ebner, W. Leitner, S. Pogatscher, Proceedings of the EMC (2019) 639–652.
[22] R. Hielscher, H. Schaeben, J Appl Crystallogr 41 (2008) 1024–1037.
[23] J. Grasserbauer, I. Weißensteiner, G. Falkinger, S. Mitsche, P.J. Uggowitzer, S. Pogatscher, Materials (Basel, Switzerland) (2020) 13.
[24] Y. Wang, Y. Deng, Q. Dai, K. Jiang, J. Chen, X. Guo, Materials Science and Engineering: A 803 (2021), 140477.
[25] F.J. Humphreys, Acta Metallurgica 25 (1977) 1323–1344.
[26] O. Engler, J. Hirsch, Materials Science and Engineering: A 336 (2002) 249–262.
[27] M.X. Guo, J. Zhu, Y. Zhang, G.J. Li, T. Lin, J.S. Zhang, L.Z. Zhuang, Materials Characterization 132 (2017) 248–259.
[28] L. Yu, L. Chen, H. Wang, X. Wang, W. Peng, Y. Wang, L. Zhuang, Metall. Res. Technol. 117 (2020) 508.
[29] L. Yuan, M. Guo, K. Yu, J. Zhang, L. Zhuang, Philosophical Magazine 101 (2021) 1417–1442.
[30] P. Ebenberger, P.J. Uggowitzer, S. Kirnstötter, B. Gerold, S. Zaefferer, S. Pogatscher, Scripta Materialia 166 (2019) 64–67.
[31] M.F. Ashby, The Philosophical Magazine: A Journal of Theoretical Experimental and Applied Physics 21 (1970) 399–424.
[32] D. Ma, Journal of Applied Physics 124 (2018) 85109.
[33] G. Taylor, Proc. R. Soc. Lond. A 145 (1934) 362–387.
[34] H. Yamamoto, Conditions for shear localization in the ductile fracture of void-containing materials, Office of Scientific and Technical Information (OSTI) (1977).
[35] A. Bjurenstedt, E. Ghassemali, S. Seifeddine, A.K. Dahle, Materials Science and Engineering: A 756 (2019) 502–507.
[36] D. Broek, Engineering Fracture Mechanics 5 (1973) 55–66.